

**Seismic Hazard Mitigation and Crustal Deformation: Results from Finite Source Process  
of Six Mw > 5.8 Chi-Chi, Taiwan Aftershocks**

Wu-Cheng Chi<sup>1</sup> and Doug Dreger<sup>1</sup>

<sup>1</sup>Seismological Laboratory, University of California at Berkeley

Index terms:

- 7215 Earthquake parameters
- 7230 Seismicity and seismotectonics
- 7223 Seismic hazard assessment and prediction
- 7294 Instruments and techniques
- 8105 Continental margins and sedimentary basins

Key words: Taiwan, Earthquake, Finite Source Processes, Basement Deformation, Strong Motion, Seismic Hazard Mitigation.

## **Abstract**

We inverted strong motion data for the finite source parameters of 6 large aftershocks of the 1999 Chi-Chi, Taiwan earthquake. For each event, we derived a preferred model by testing different focal mechanisms, hypocenters, rupture velocities, and dislocation rise times, as well as different combinations of stations in more than 1000 inversions. We documented how the fits between the waveforms and the corresponding synthetics deteriorated as the hypocenter and focal mechanism deviate from those of the preferred model. These results will help to determine how accurate these parameters must be if we wish to derive slip models in near real-time for generating shakemaps. If the deviation in focal mechanisms and hypocenters were less than  $20^\circ$  and 5 km, respectively, we generally recovered 80% of the preferred model's synthetic waveform fit. Unlike the dislocation rise time, the rupture velocity used in the inversion had a strong influence on the waveform fits. We also used the slip models to study fault geometry. Two of the aftershocks ruptured on the southern extension of the mainshock fault plane. One strike-slip aftershock nucleated within the basement but ruptured mainly within the overlying sedimentary strata, suggesting that seismogenic deformation in the basement can influence shallow structures. P-axes of the derived models have azimuths consistent with current plate motion. Finally, GPS displacement derived from the 6 slip models can explain 80% of the post-seismic deformation observed in the aftershock regions, indicating that studies of post-seismic deformation must take into account the cumulative effects of large, shallow aftershocks.

## **Introduction**

More than 30,000 aftershocks occurred in the three months following the Chi-Chi,

Taiwan earthquake ( $M_w=7.6$ ). Among them, more than 6 aftershocks with  $M_w>5.8$  were well-recorded by a strong motion network maintained by the Central Weather Bureau of Taiwan.

They provided an unprecedented opportunity to study the finite source process of moderate sized earthquakes 1) to learn more about the spatial relationships of faults in the region, 2) to compare source parameters of the moderate to large aftershocks with those of the mainshock, and 3) to map the deep crustal structure of Taiwan.

Here we document finite source inversions and sensitivity tests for 6 of the aftershocks (table 1) for which strong motion data are available. Each aftershock was recorded by more than 200 strong motion stations. We use only data from stations that had no apparent timing errors and provide good azimuthal coverage (Figure 1). Using a preliminary slip model, for each event we tested a range of values for each of the source parameters: the slip vector, fault orientation, location, hypocentral depth, rupture velocity, and dislocation rise time. In this modeling we assumed that the rupture velocity and dislocation rise time were constant and did not vary spatially. For each event, we performed more than 1000 sensitivity tests by varying the source parameters used in the inversions and we documented the influence these parameters have on the slip model and the waveform fits (table 2). To determine what the contributions of individual stations are and whether the results might be biased, we applied “Jackknife tests.” That is we examined the fits of the waveforms from the inversions for which we excluded the data from one station at a time until we have tested all the stations in the preferred model. With these tests we were able to derive a preferred slip model that was stable and gave good waveform fits. As none of these aftershocks ruptured the surface, nor had rupture planes unambiguously defined by smaller aftershock seismicity, these inversions were also used to determine the orientation of the

causative plane and to provide an estimate of the confidence in the chosen plane.

The Chi-Chi sequence also provides a great opportunity using earthquake sources to map the deep crustal structures of Taiwan. Several seismicity and moment tensor studies have already illuminated the geometry of important seismogenic faults at depth (e.g. Kao and Chen, 2000; Hirata et al., 2000, Carena et al., 2002, Chen et al., 2002). To make the tectonic interpretation easier, we want to connect these data "points" in three dimensions using the planes of the planar slip models derived from the results of our finite fault inversion. The mainshock and aftershock slip models then can also be used to calculate the static stress perturbation during the entire earthquake sequence.

All of these results are important for seismic mitigation. The causative faults derived from this study, all of which are blind, can be added to the map of active faults in Taiwan. The stress perturbation from mainshock and aftershocks can be used to recalibrate the post-seismic regional stress pattern. The slip models are important for studying earthquake source scaling relationships and attenuation relationships for engineering purposes. Also, the extensive sensitivity tests document how variations in the input source parameters affect the waveform fits derived from the finite fault inversions. As a result, these studies provide the criteria needed to evaluate the performance of the seismic network if we want to invert the finite fault parameters in real time and use the source model to forward-model the shakemaps, which can be used by the seismic response authorities for seismic mitigation purposes (e.g. Dreger and Kaverina, 2000).



## **Regional Tectonic Setting of Taiwan**

Central Taiwan is located in the collision zone between the Luzon arc of Philippine Sea plate and the Chinese passive margin of the Eurasia plate. The relative plate motion is about 80 mm/yr in the N66°W direction (Yu et al., 2001). Here the Chinese continental passive margin, with normal and strike-slip fault structures, enters into the convergent boundary where contractional processes dominate. Suppe (1981) has proposed that most of the sediments above the basement are being incorporated into the Taiwan fold and thrust belt by westward propagation of a low angle east-dipping decollement fault, beneath the mountain belt. However, the shortening style below the decollement is less understood. The basement may act as a relatively rigid body underthrusting the mountain belt (Suppe, 1981; Suppe, 1984) or it may deform internally to thicken the crust in Taiwan (Rau and Wu, 1995).

## **Chi-Chi, Taiwan, Earthquake and Its Aftershocks**

Seismicity and moment tensor studies of the Chi-Chi earthquake sequence have already provided important constraints on the crustal geometry. Kao and Chen (2000) proposed that the aftershocks occurred on two parallel, low-angle east-dipping faults, one in the vicinity of the proposed decollement and a second 15 km below it (Figure 1a, inset). The decollement is also illuminated in an aftershock study by Hirata et al. (2000), although with a shallower dip. Carena et al. (2002) suggested a low-angle east-dipping detachment under most of central and eastern Taiwan, with a separate seismicity zone underneath the detachment dipping to the west. Chen et al. (2002) present evidence for this west-dipping seismic zone based on their relocations of

events and the focal mechanisms they determine (c.f. the basement-involved west-dipping fault in Figure 1a). Overall, the aftershocks are well-located. However, the uncertainties in focal depths and the ambiguity in determining the causative fault planes from moment tensor or first-motion solutions have prompted different interpretations of the fault geometry. In addition, some of the large aftershocks in the vicinity of the decollement consistently have one nodal plane dipping  $30^\circ$  to  $40^\circ$  to the east (e.g. Kao and Chen, 2000), which is steeper than the proposed shallowly dipping decollement. As a result, these aftershocks could have ruptured either on the shallowly dipping decollement, on the west-dipping backthrusts above the decollement, on the steeper east-dipping splay faults above the decollement, or even on steep west-dipping basement-involved reverse faults under the decollement (Figure 1b, inset).

The finite-source process of the mainshock has been studied extensively using various combinations of strong motion, teleseismic, and GPS data (e.g. Yagi and Kikuchi, 2000; Kikuchi et al., 2000; Ma et al., 2000; Ma et al., 2001; Zeng and Chen, 2001, Mori et al., 2000; Ji et al., 2001; Wu et al., 2001; Chi et al., 2001; Lovenbruck et al., 2001, Johnson et al., 2001). To a first order, the source models are all consistent, showing large slip to the north of the focus at shallow depths. Slip to the south tends to be less constrained. There is evidence that the extent of mainshock rupture may have been structurally controlled and Chi et al. (2001) suggest that the mainshock asperity terminated in the south along a lineation between the towns of Puli and Chusan (Figure 1).

Excellent GPS displacement data have been collected for the pre-event, coseismic, and postseismic epochs (Yu et al., 2001). More than 10 m of horizontal co-seismic displacement was

found in the northern region of the surface rupture. There are also greater than 10 cm of displacement recorded 3 months after the mainshock, mostly in the southern section of the surface rupture (Hsu et al., 2002), where the large aftershocks occurred.

### **Strong Motion Data and Method**

In this study we use strong motion data collected by the Central Weather Bureau (CWB) of Taiwan (Lee et al., 2001) and supplement it with data from the Institute of Earth Sciences (IES), Academia Sinica of Taiwan. Overall, more than 200 accelerometers with sample rates of either 200 or 250 sps, recorded each of the six large aftershocks. We have converted each waveform from digital counts to  $\text{cm/s}^2$ , removed the mean offset, integrated from acceleration to velocity, and bandpass filtered between 0.02 and 0.5 Hz with a four-pole acausal Butterworth filter before resampling the data to 10 sps.

Using a frequency-wave number code from Chandan Saikia (Saikia, 1994), we calculated a catalog of Green's functions for an average 1D velocity model (table 3) taken from a 3D tomographic study by Rau and Wu (1995). This 1D model had been tested in routine regional moment tensor studies of local and regional events (c.f. Kao and Chen, 2000) and performed well for the finite fault inversions of Chi-Chi mainshock (Chi et al., 2001) and aftershock (Chi and Dreger, 2002). The Green's functions were subjected to the same signal processing.

We used strong motion data to invert the representation theorem, equation 1 (Aki and Richards, 1980), for parameters of the finite source using a method pioneered by Hartzell and

Heaton (1983). The seismograms are used to calculate the spatio-temporal integration of slip distribution on a plane where,

$$u_n(x, t) = \int_{-\infty}^{\infty} d\tau \iint_{\Sigma} [u_i(\xi, \tau)] c_{ijpq} v_j \partial G_{np}(x, t - \tau; \xi, 0) / \partial \xi_q d\Sigma \quad (1)$$

$u_n$  nth component of observed velocity

$c_{ijpq}$  fourth-order elasticity tensor

$v_j$  fault orientation unit vector

$G_{np}$  Green's function

$x$  vector describing the relative location of the source and receiver

$\xi, \tau$  spatial and temporal variables of integration

In the equation,  $n$  refers to the ground motion component and  $i, j, p,$  and  $q$  are orientation indices. The quantity  $u_i(\xi, \tau) c_{ijpq} v_j$  is equivalent to  $m(\xi, \tau)$ , the seismic moment tensor which changes in space and time.  $u_i(\xi, \tau)$  is the spatio-temporal slip information to be determined by inverting the data.

We use a damped, linear least-squares inversion to determine the spatio-temporally discretized slip. For each grid point (subfault) on the gridded fault plane, we calculate the slip amplitude using a prescribed slip vector direction. We use a single time-window with a fixed dislocation rise time propagating away from the hypocenter with a spatially constant rupture velocity, due to the relatively small magnitude of the aftershocks compared with the mainshock.

The absolute times of the waveforms were tested by aligning the data with the Green's functions in time. Laplacian smoothing and moment minimization constraints, as well as slip positivity, implemented using the non-negative least squares inversion of Lawson and Hanson (1974), are used as constraints to improve the stability of the inversions.

A range of values for the following source parameters (table 2) have been tested to see their effects on the inverted synthetics and to improve the waveform fits: hypocentral locations, rupture velocity, dislocation rise time, focal mechanism on both conjugate fault planes. By doing this we were able to identify which parameters have stronger influence on the inversions.

Due to the vast amount of strong motion data, and the uncertainty about the accuracy of the timing at some stations, we expended a great deal of effort to find the optimal station configuration. The waveform fits for the initial inversions are usually not good, especially if some seismograms have apparent timing errors or large amplitude phases due to crustal 3D velocity heterogeneity. The waveform fits also degraded if the source parameters used in the inversions were not close to those of the preferred model. To avoid timing problems, we picked stations with arrival times similar to the arrival time predicted by our 1D velocity model, as was done in Chi et al. (2001). Horizontal particle motion for each station was plotted in map view to help identify and avoid stations with abnormally large particle motion compared with neighboring stations (Figure 2). To characterize the ground motion in urban regions during the aftershocks, we also used these particle motion plots to document horizontal peak ground velocity (HPGV) direction and the aspect ratio between the short and long axes (Figure 2). For each aftershock, we have tested all of the available moment tensor solutions, some of which have

very different focal mechanisms and source depths. Using the reported moment magnitude, we parameterized the fault dimensions, and dislocation rise times using the relationships published by Sommerville et al. (1999). If necessary, we adjusted the fault dimensions for each individual aftershock. In some cases the dimension of the fault model was too small, so the slip terminated at the edge. We then had to increase the fault dimension. In other cases, when the initial dimensions of the fault were too large, some energy from later parts of the waveforms were mapped into the slip model, even though they might have been scattered wave fields and not related to the earthquake source. We then reduced the size of the fault.

Once we had an initial model with an optimal configuration of stations, we did a grid-search over a range of source parameters, including the direction of the slip vector, the fault orientation, the hypocentral location, the rupture velocity, and the dislocation rise time (table 2). We varied these source parameters one at a time, running the inversion using the new input parameter, and then studied the changes in slip model and waveform fits. Thus we were able to document the sensitivity of the synthetics and their fits to the waveforms to each of these parameters before selecting the preferred model. In doing so, we were able to improve the waveform fits and estimate the uncertainty in each of the preferred source parameters. For this purpose we define the error bounds as 10% of the variance reduction (VR) [ $VR = 1 - (\sum(\text{synthetics} - \text{data})^2 / \sum(\text{data})^2)$ ] from the preferred model. To test the contribution of some individual seismic stations to the preferred model, we then excluded these stations and reran the inversions to document the change in the slip models and waveform fits. For each event, we did more than 1000 tests; each taking 10-20 minutes on a typical SUN workstation. We then assigned confidence levels for the preferred slip model based on waveform fits and by comparing

the results with other geologic and geophysical data. While these sensitivity tests only covered a small portion of the total parameter space, this study represents the most thorough attempt to document such uncertainties in finite source inversions.

### **Finite Fault Inversion For Event 1 (09201757)**

Event 1 occurred on 20 September 1999, 17:57:15.31 UTC, and was located at 121.01°E, 23.94°N at a depth of 8 km (Figure 1b). Its strike, dip, and rake are 200°, 41°, and 78°, respectively. The moment and  $M_w$  are  $7.15 \times 10^{24}$  dyne-cm and 5.8, respectively. We have low confidence in the preferred model (Figure 3) for this event, which occurred 10 minutes after the mainshock at a time when many other aftershocks were occurring. Horizontal peak ground velocity (HPGV) at some stations is polarized E-W but most of the other stations do not have a consistent HPGV direction. A  $M_L=4.61$  event occurred 23 km away and 1 sec before this event, thereby complicating the preliminary estimation of hypocentral parameters (Gensin Chang, personal communication, 2002), and thus the finite fault inversion. Sensitivity tests show that the 12 km by 4 km rupture patch is located near 121.04°E, 23.97°N. Its depths range from 6 to 8 km, shallower than the proposed decollement. Our slip model has a maximum slip of 46 cm while the static stress drop is 5.3 MPa. The variance reduction (VR) of the derived preferred model determined using data from thirteen 3-component stations is 46%, slightly less than the VR of 48% for the east-dipping conjugate fault. We favor the west-dipping fault plane because it correlates well with the locations of the aftershocks (Figure 3). To identify stations that will help determine the causative fault plane, we forward-predicted ground motions using both conjugate fault slip models and found that both models can fit most of the near source stations

relatively well, partly because three near source stations were used in the inversion to constrain the models. However, the two conjugate slip models produced very different synthetics east of the hypocenter in the mountainous regions where strong motion data are not currently available. Thus, good station coverage in the mountainous region above the decollement will be important for future finite source studies.

Using a 10% decrease in VR as the error threshold, we found that a location error less than 4 km still gave a good fit to the waveforms (Figure 1b). Within 20° of error in focal mechanism is also acceptable, as shown in Figure 4. Possible focal depths range from 6 to 13 km, and rupture velocities from 1.3 to 2.6 km/s (Figure 5). Waveform fits are not very sensitive to dislocation rise time. Table 1 lists details of the source parameters and slip models of each of the events.

### **Finite Fault Inversion For Event 2 (09201803)**

Event 2 occurred on 20 September 1999, 18:03:41.16 UTC and was located at 120.86°E, 23.81°N at a depth of 8 km (Figure 1b). The strike, dip, rake are 0°, 10°, and 80° respectively. The moment and Mw are  $2.53 \times 10^{25}$  dyne-cm and 6.2, respectively. We assign a high level of confidence to the preferred model (Figure 6) for this event and the VR from the inversion of data of thirteen 3-component stations is 56%. The preferred model is strongly controlled by station TCU079 because the VR of the inversion removing this station from the optimal station configuration drops to 50%. The mapview plot of particle-motion shows a clear westward thrust radiation pattern. The back-azimuth direction is mostly sub-parallel to the HPGV direction. As



a result, there is generally more E-W ground motion on the western coastal plains, which are densely populated. The particle motion shows an aspect ratio of 1:2 between the short and long axes. Some secondary phases, recorded 20 seconds after the origin time (i.e. at stations TCU078, TCU079, TCU089), could not be modeled in our inversions. These late arrivals do not contribute to the preferred slip model. The 10 km by 10 km slip patch is located near 120.82°E and 23.79°N at a depth of 6 to 8 km. Maximum slip is 231 cm and the static stress drop is 6.2 MPa. This aftershock ruptured along the southern end of mainshock asperity along the Puli-Chusan lineation proposed by Chi et al. (2001). In the cross section view, our slip model coincides with the shallowly east-dipping fault imaged by a recent reflection profile from Wang et al. (2002). Because the dip angle is very shallow, we suspect that there may be trade-offs between strike and rake. For example, a slip model with a strike and rake of 350° and 80° will be similar to that of 20° and 110° because the slip at each subfault of both models will have similar azimuths and the latitude and longitude. The low slip near the hypocenter (Figure 6) may be an artifact resulting from an incorrect origin time. However, we tested this by adding a delay of less than 1 sec to the reported origin time. While the slip became more concentrated near the hypocenter, waveform fits were degraded. To be consistent with other events in this study, we continued to use the reported origin time. Sensitivity tests of focal depth, rupture velocity, and dislocation rise time have patterns similar to that of Event 1.

### **Finite Fault Inversion For Event 3 (09202146)**

Event 3 occurred on 20 September 1999, 21:46:37.49 UTC at 120.82°E, 23.60°N at a focal depth of 18 km (Figure 1b). The strike, dip, and rake are 330°, 89°, and 15°, respectively.

The moment and  $M_w$  are  $2.2 \times 10^{25}$  dyne-cm and 6.2, respectively. We assign a high level of confidence to the preferred model for this event, which has a VR of 56% from the inversion of nine 3-component stations. Unlike the other thrust-type aftershocks, this strike-slip event has N-S oriented HPGV direction in the coastal plain, perpendicular to the back azimuth direction and consistent with a strike-slip radiation pattern for the S wave. The aspect ratio for the horizontal particle motion plot is about 1:3 to 1:4 at most stations. The 5 km by 25 km slip patch on a vertical plane mainly ruptured in sedimentary units at depths similar to that of the Event 2 slip patch. The maximum slip is 85 cm (Figure 7), and the static stress drop is 3.8 MPa, the lowest among the aftershocks we studied. Location tests show that hypocenters within an elongated region along the strike of the fault gave good waveform fits (Figure 1b). The preferred rake is similar to the dip of the decollement to the north, consistent with the kinematics north of this strike-slip fault. A depth of 18 km places the hypocenter in the basement.

We have studied the relationship between waveform fits and the hypocentral depth assigned in the inversions. For this event, the variance reduction decreased 10% when we used a hypocentral depth of shallower than 10 km (Figure 5). In particular, the inversions with shallow hypocenters could not generate the large amplitude particle motion observed at stations CHY080 and CHY035. Our slip model is strongly controlled by station CHY080. When it is omitted from the inversion, the VR actually decreases by 12%. The amount of slip in the basement depends slightly on the level of smoothing and on moment minimization constraints, but the overall "belt-shaped" slip patterns in the basement are similar. The fault slip is near two of Taiwan's highest mountains, and the waveforms could be complicated due to scattering of the wavefield from the rough topography. This event occurred on a fault not previously mapped. However, this NW-EW striking fault is parallel to and located between two other faults shown

on the geologic map (Central Geological Survey, 2000), which, like this slip model, are bounded at both ends by two NE-SW trending faults.

#### **Finite Fault Inversion For Event 4 (09220014)**

Event 4 occurred on 22 September 1999, 00:14:40.77 UTC at 120.08°E, 23.81°N at a depth of 10 km (Figure 1b). The strike, dip, and rake are 165°, 70°, and 100°, respectively. The moment and Mw are  $2.5 \times 10^{25}$  dyne-cm and 6.2, respectively. We assigned a low confidence level to the preferred model for this event. The VR for data from nine 3-component stations is 48% (Figure 8). Station configuration tests show that the slip model is not dominated by any one station. Its HPGV direction is mainly EW in the western coastal plain. Most of the horizontal particle motion has an aspect ratio of 1:4. In contrast to most of the other aftershocks, some stations on the east coast of Taiwan recorded amplitudes larger than those of western stations at similar epicentral distances. A wide range of focal mechanisms have been reported for this event (table 1) and reported epicentral depths range from 12.4 to 29 km (Chen et al., 2002; ERI website; Harvard CMT; Kao and Angelier, 2001). Sensitivity tests show that the 6 km by 20 km slip patch is located near 121.04°E, 23.85°N with depths ranging from 13 to 24 km. This aftershock ruptured downdip into the basement. Our slip model has a maximum slip of 83 cm and a static stress drop of 4.6 MPa (Figure 8). It was difficult to interpret which of the conjugate fault planes ruptured due to the uncertainty in the focal depth of this event. The preferred models for both of the conjugate faults give VRs greater than 40%. But they favor different focal depths and rupture velocities (Figure 5). If the focus is deep and the rupture velocity very slow, it is possible to fit the waveforms well with the east-dipping fault. However smaller

aftershocks correlate better with the steep west-dipping fault, not the east-dipping fault above the decollement. Our result is more consistent with the west-dipping seismicity below the decollement observed by Carena et al. (2002), and Chen et al. (2002). The strike of this slip model shows 30 degrees difference from that of seismicity from Carena et al. (2002) but is consistent with the focal mechanism of Chen et al. (2002).

### **Finite Fault Inversion For Event 5 (09252352)**

Event 5 occurred on 25 September 1999, 23:52:49.51 UTC at 121.01°E, 23.87°N at a depth of 16 km (Figure 1). Its strike, dip, and rake, 5°, 30°, and 100°, respectively, are very similar to those of the mainshock. The moment and  $M_w$  are  $3.7 \times 10^{25}$  dyne-cm and 6.3, respectively. We have high confidence in the preferred solution for this event because the VR from the inversion of data from eleven 3-component stations is 72% (Figure 9). The slip model is strongly controlled by station TCU078. Chi and Dreger (2002) published preliminary finite fault inversion results for this event. Here, we have performed additional sensitivity tests and included them for completeness. The HPGV direction is mainly E-W in the western coastal region, and the particle motion aspect ratio is mostly 1:4. Waveforms recorded southwest of the epicenter had large amplitudes. The 6 km by 22 km slip patch is near 121.00°E, 23.81°N with depths from 12 to 18 km. Our slip model has a 162 cm maximum slip and a static stress drop of 5.9 MPa (Figure 9). In map view and in cross section this event appears to be a down-dip extension of Event 2, although the dips of the two events are slightly different. Due to the uncertainty in depth and the steeper dip angle, this event may have been on a step down of the decollement or a splay fault above it. Both events ruptured along the Puli-Chusan Lineation and

are sandwiched between aftershock seismicity to the south and mainshock rupture to the north.

### **Finite Fault Inversion For Event 6 (10220218)**

Event 6 occurred on 22 October 1999, 02:18:56.93 UTC at 120.45°E, 23.53°N at a depth of 16 km (Figure 1b). It caused at least 12 buildings to collapse near the city of Chai-Yi. The strike, dip, and rake are 20°, 75°, and 90°, respectively. The moment and  $M_w$  are  $1.7 \times 10^{25}$  dyne-cm and 6.1, respectively. The VR is 60% from the inversions of data from fourteen 3-component stations. Because fits from both conjugate faults were equally good, we assigned a low level of confidence to the preferred model for this event. More than 30 strong motion stations at epicentral distance less than 25 km recorded this event, and at all azimuths.

The near source waveforms may have been complicated by 3D basin structures, which may explain the wide range of MT solutions and differences of up to 5 seconds in origin time reported by different agencies (table 1). Overall the HPGV direction is WNW-ESE east and west of the hypocenter and N-S for stations south of hypocenter. In a preliminary finite fault inversion using data from 6 strong motion stations, the west-dipping fault produced better variance reduction. By adding 8 additional stations in the course of station configuration tests, we found that the variance reduction of the west-dipping plane is slightly higher if the focal depth is about 8 km. However, the east-dipping plane also produced good waveform fits if we used a focal depth of 16 km (Figure 10). We picked the east-dipping fault plane as the preferred model only because most of the focal depths reported for this event are consistently around 16 km and regional geologic interpretation favors east-dipping faults.

## **Sensitivity of the Inversions to the Station Used and to Changes in the Source Parameters**

Because more than 200 stations recorded each aftershock, the most challenging part of this study was to find the configuration of stations which gave good azimuthal coverage and enough waveforms with paths that could be represented by the simple 1D crustal model we used to calculate the Green's functions. Many of the strong motion stations may have timing problems (Lee et al., 2001) and may be affected by the 3D heterogeneity of velocity structures along the path. If we randomly selected 20-40 stations with good azimuthal coverage and inverted them, the resulting scalar moments were small and the variance reduction low. For this particular study, we chose to use between 9 and 14 stations. We picked the stations by trial and error and by eliminating stations with abnormal waveforms compared to neighboring stations. In particular, we chose stations based on their performance in initial inversions using preliminary source parameters derived from those reported by various agencies, thus the selection of stations may be biased if the reported source parameters are incorrect. To make our analysis more robust, we made a concerted effort to test any newly reported source parameters as they became available.

The focal mechanism is one of the most important source parameters in our inversion. We did a grid search on the focal mechanism parameters and found that, overall the waveform fits are strongly controlled by the dip angle. A deviation of  $20^\circ$  will decrease the VR by 10% (Figure 4), e.g. VR will decrease from 50% to 40%. However, the single strike-slip event among these aftershocks is more sensitive to strike and rake than the thrust events. This may be

related to the fact that the maximum amplitude of the shear wave radiation patterns coincides with the fault planes. As a result, the large amplitude waveforms are up-dip of the thrust and along a strike-slip fault, and are sensitive to the dip of the thrust or the strike of the strike-slip fault, provided the hypocenter is fixed. For strike-slip faults, this poses only a small problem because their causative faults can usually be identified easily by aftershock distributions, which usually have epicentral locations that are more accurate than their depths. However, for blind thrusts, it is possible that discrepancies in the dip of preliminary focal mechanisms maybe up to  $20^\circ$  and this could cause problems for routine finite source inversions that rely on an a priori knowledge of the fault orientation.

Good hypocentral information is also very important. We found that the epicentral location has a large influence on the waveform fits (Figure 1b). When we shifted the hypocenter by 5 km from the optimal hypocenter, the VR of the synthetics decreased about 10%. Except for Event 4, we also found that an error of 5 km in focal depth will reduce the VR by 10%. For comparison, the asperities we derived from this study have dimensions ranging from 5 km by 10 km to 6 km by 22 km. So the error bounds are roughly similar to the small dimension of the slip distribution.

More accurate focal depths would be helpful in cases where we not only want good waveform fits, but also want to determine the causative fault for thrust events such as these with  $M_w$  ranging from 5.8 to 6.3. Overall, the inversion will place the slip at a location and at an elapsed time from origin time (Figure 11). For updip or downdip ruptures this means that, for a fixed hypocentral location, one hypocenter will be shallower than the slip depth while the

conjugate fault scenario will have a hypocenter deeper than the slip depth. Provided that the Green's functions and the inversions have placed the slip patch at the correct location and depth, an accurately reported hypocentral depth will help determine which fault plane has ruptured. The locations of smaller events, aftershocks of the large aftershocks, can also help to constrain the causative plane.

From sensitivity tests we found that the optimal rupture velocity depends on the dip angle of the fault plane, and on the relative location of the hypocenter and major slip (Figure 11). Again we must assume that the origin time of the event and the Green's functions are correct. Then the inversion will place the slip at a specific location and at a specific time. To get good waveform fits, the optimal rupture velocity must be the ratio between the distance from the hypocenter to the slip (rupture distance) and the lapse time. For a fixed hypocentral location, the more steeply dipping fault of the two conjugate planes will have a longer rupture distance, and thus a higher optimal rupture velocity. This analysis suggests that the rupture velocity may help to further constrain the causative fault plane. Using Event 4 as an example, we found the slip model on a  $70^\circ$  west-dipping fault plane gave a reasonable rupture velocity while the  $20^\circ$  east-dipping fault plane gave a very low rupture velocity. This result is consistent with the interpretation that this event ruptured on the west-dipping fault.

Compared to the tests of focal mechanisms and hypocentral locations, we found that the inversions are not very sensitive to changes in the dislocation rise time. This is, in part, due to the relatively small size of the events and the low pass filter-corner applied to the data and Green's functions. Empirical relationships indicate that the average rise times for such events



should be short, at or below limit of resolution of our tests.

## **Implications for Seismic Hazard Mitigation**

Recently there has been a push within the seismological community to produce maps of ground shaking intensity in near real time for emergency response purposes (e.g. Wald et al., 1999). In densely instrumented regions, such as Southern California, Japan, and Taiwan, these maps can be generated using ground-truth measurements. However, other approaches are needed for regions with sparse station coverage, including an approach to derive finite source parameters in near real time, then forward model the ground shaking in the regions of interest (e.g. Dreger and Kaverina (2000)). An initial set of good source parameters will dramatically reduce the time required to derive a slip model and enable us to generate synthetic ground shaking information in a timely fashion. It is also beneficial to have correct finite source information soon after the earthquake. The information then can help to identify the causative fault plane, design temporary portable seismic networks to monitor the aftershocks surrounding the main event, and forward calculate the stress perturbation due to the earthquake.

We found that it is important to identify several good stations, which can be used for initial finite source inversions. Using all of the available stations can sometimes overwhelm the inversion, and useful information in the waveforms may be suppressed due to timing problems and site effects.

To successfully predict ground motion we need to have good waveform fits at all

azimuths from the hypocenter. From our sensitivity tests on  $M_w=5.8-6.3$  earthquakes we found that this can be easily achieved if the hypocenter mislocation is less than 5 km and if the focal mechanisms are accurate to within  $20^\circ$ . Such epicentral accuracies are found, for example, within the error estimates from 90% of the 1590 earthquakes (1998-2002) in the Northern California Earthquake Data Center Hypocenter 2000 Catalog available at <http://quake.geo.berkeley.edu/ncedc/catalog-search.html>. Damaging earthquakes may have surface ruptures that can be reported within a short period of time.

### **Implications for Regional Tectonics**

We have proposed that two of the aftershocks discussed here occurred in the vicinity of the proposed east-dipping decollement, one west-dipping backthrust event ruptured above the decollement, one strike-slip aftershock nucleated in the basement then ruptured through the overlying sedimentary layers, and two of the shocks occurred on basement-involved reverse faults (Figure 1b).

The two aftershocks in the vicinity of decollement ruptured along the Puli-Chusan lineation (Figure 11). In cross section these two aftershocks form a flat-ramp geometry. However, given the uncertainty in depth, Event 4 could have been at a shallower depth becoming a splay fault branching up from the decollement.

The west-dipping backthrust slip model above the decollement from Event 1 was

assigned low level of confidence. Combined with the east-dipping decollement that ruptured during the mainshock, this west-dipping backthrust aftershock forms a pop-up structure, such as proposed to explain the pure shear type of microstructure deformation observed in the mountains to the north (Clark et al., 1993). Sandbox modeling by Lu et al. (2002) also predicted backthrusting in this region.

Two of the aftershocks show basement-involved reverse faulting. Although both of them were assigned low confidence levels, the deep focal depths determined from our analysis are robust, as inversions using shallow focal depths could not generate satisfactory waveform fits. The steep dip angles of our preferred fault models suggest that these events ruptured on pre-existing weak zones, presumably a steeply dipping normal fault along the passive margin. In fact, many studies have proposed reactivated normal faults in this region based on oil company reflection data and well log data (e.g. Suppe, 1984). Our results suggest that such structures may currently be seismogenic.

Though assigned a low confidence level, our slip model for Event 4 is a west-dipping fault under the decollement, which is consistent with the results from Carena et al. (2002) and Chen et al. (2002). Repeated west-dipping reverse faulting events under the decollement could uplift the western part of the decollement over a long period of time. Thus if the regional decollement is flat in this region (Carena et al., 2002) or only dips slightly to the south (Wang et al., 2002), this type of basement reverse faulting could be a transient or young feature. Another possibility is a duplex style of deformation between two sub-horizontal main detachment faults. If the causative plane dips to the east, the preferred slip model will be more consistent with the

sub-parallel fault model from Kao and Chen because the alternative preferred model has a focal depth of 25 km (Figure 1a).

Event 6 occurred on a basement-involved reverse fault under the eastern plains. Although at greater depth, basement faults in this region can pose significant seismic hazard because they lie directly beneath cities. The strike of this fault is sub-parallel to the topographic lineation further to the east (Figure 12). Like other basement-involved aftershocks in this study, this aftershock's fault plane may be controlled by the structures in the underthrusting passive margin. If the earthquake ruptured on the west-dipping fault plane, our analysis shows that the preferred focal depth is about 8 km, which is within the basement.

Event 3 is a strike-slip event initiated within the basement but the asperity is mostly concentrated at shallow depth along and above the proposed decollement. In fact the slip seems to have a rake consistent with the shallow dip of decollement 5 to 10 km to the north. Our result provides evidence of basement deformation propagating to the overlying sedimentary layers and generating large slip at shallow depth. If true, this will be one of the first studies that show deformation style above the decollement being influenced by active deformation within the basement. Because of the shallow asperity, we predicted that deformation may be detectable in GPS measurements.

Except for Event 4, the azimuths of the P axes derived from our preferred models are roughly about N70°E (Figure 4), consistent with the current relative plate motion. However, the fault plane orientations of these 6 aftershocks are very different. This suggests that the

kinematics of these large aftershocks is mainly controlled by tectonic stress, although they occurred on pre-existing weak zones that do not have similar attitudes. The triggering of the aftershocks may be closely related to stress perturbation due to the mainshock rupture, suggested by the static stress transfer study of the mainshock (Wang et al., 2001) and by Kao and Angelier (2001) based on moment tensor data.

Post-seismic deformation has been studied extensively for recent large earthquakes (e.g. Bürgmann et al., 2002). There is an excellent post-seismic GPS dataset (Hsu et al., 2002) for the Chi-Chi earthquake sequence. Chi and Dreger (2002) documented the large contribution from Event 5 to the post-seismic deformation, composing up to 30% of the total post-seismic displacement at several stations near this event. Here we forward-predicted the GPS deformation using a half-space elastic structure (Okada, 1992) for the slip models of the 6 aftershocks. The cumulative aftershock-related displacement from these 6 aftershocks was as high as 10 cm at some GPS stations, explaining at least 80% of the post-seismic deformation observed in the southern half of the hanging block where these aftershocks occurred (Figure 13).

## **Conclusion**

We have inverted strong motion data to determine the finite source parameters for six large aftershocks of the 1999 Chi-Chi, Taiwan earthquake sequence (Figure 12). Of these events, five showed dip-slip motion and one was strike-slip in nature. We tested more than 1000 inversions for each event and documented the variation in the waveform fit due to different input parameters, including changes in the station configuration, the focal mechanism, the hypocentral

location, the rupture velocity, and the dislocation rise time. We then assigned confidence levels for each event based on these tests and by comparing the resulting slip models with other geologic and geophysical data.

Three of the aftershock slip models were assigned high levels of confidence due to good waveform fits and good correlation with results from reflection data, seismicity, and geologic maps. Particularly, the slip model for Event 2 correctly depicted the fault orientation imaged by recently released reflection data.

Except for one strike-slip event, which started deep, and one event located to the west in the footwall of the mainshock, the ruptures of the other events began in the vicinity of the decollement near the mainshock slip. We have high confidence in the slip models that ruptured updip on the decollement. However, there is also strong evidence of updip rupture to the east, forming a pop-up structure, or downdip rupture to the west below the decollement, suggesting some of the four aftershocks may not have ruptured on the proposed decollement.

We use the sensitivity test results to place bounds on the source parameter space that will give relatively good waveform fits. In another words, we have tested different input parameters to determine their influence on inversion results for these Mw 5.8-6.4 earthquakes in Taiwan region. We found that inversions using 10 stations usually gave stable results, provided there are no timing errors. Jack-knife tests show that with fewer stations we can still derive similar slip models, but the results are not as robust. The accuracies of the focal mechanism determinations have a strong influence on the waveform fits and the slip model. Particularly for the thrust

events, the input dip angle must be correct to within  $20^\circ$ , otherwise the variance reduction drops by as much as 10%. For the single strike-slip event, the strike must also be within  $20^\circ$  of the true strike. Hypocentral locations must be within 5 km of the actual locations, which is close to the smaller dimension of the slip patches we modeled. In some cases we found that to correctly determine the causative fault, we need more precise hypocentral information. Our results suggest that the rupture velocity can trade-off with the dip angle of the causative fault plane chosen and that the inversions are not very sensitive to the dislocation rise time. Although these may not be general results, this study does show that there can be significant trade-offs between the fixed parameters of the inversion and that they can bias the results.

Our results provide more detailed spatial resolution of the slip compared with the moment tensor results. Two of the aftershocks ruptured along the Puli-Chusan lineation, where the mainshock rupture stopped. Three of the aftershocks show evidence of basement-involved deformation. In particular, we found a strike-slip event that nucleated within the basement but the asperity is mainly located within the overlying sediments, strongly suggesting that basement structures play an important role in surface deformation. Five out of the 6 slip models have P-axes with azimuths consistent with current relative plate motion. However, the fault orientations of these aftershocks are very different. We interpreted this to mean that large aftershocks are triggered by the stress perturbation of the mainshock on pre-existing structures. However, the kinematics of the aftershocks remains consistent with regional tectonic stress.

### **Acknowledgments.**

We thank Dr. Willie Lee for providing the strong motion data from Central Weather Bureau

(CWB) of Taiwan and Dr. Win-Gee Huang for the strong motion data from IES, Academia Sinica of Taiwan. Dr. S.-B. Yu is thanked for providing post-seismic GPS data. We appreciate Dr. Honn Kao for his seismicity data. We thank CWB for providing their aftershock seismicity data and Dr. C.Y. Wang of National Central University for providing reflection data. We thank Dr. Peggy Hellweg and Dr. Donald Reed for their constructive comments. This research is funded by NSF Grant EAR-0000893 and PEER Lifelines 1E06.

### References:

- Aki, K, and Richards, P.G., *Quantitative seismology*, W.H.Freeman & Co., 1980.
- Buergmann, Roland, S. Ergintav, P. Segall, E.H. Hearn, S.C. McClusky, R.E. Reilinger, H. Woith, J. Zschau, Time-dependent distributed afterslip on and deep below the Izmit earthquake rupture, *Bull. Seism. Soc. Am.*, 92, 126-137, 2002.
- Carena, Sara, John Suppe, and Honn Kao, Active detachment of Taiwan illuminated by small earthquakes and its control of first-order topography, *Geology (Boulder)*, 30(10), 935-938, 2002.
- Chen, Kou-Cheng, Bor-Shouh Huang, Jeen-Hwa Wang, and Horng-Yuen Yen, Conjugate thrust faulting associated with the 1999 Chi-Chi, Taiwan, earthquake sequence, *Geophy. Res. Lett.*, 29(8), doi:10.1029/2001GL04250, 2002.
- Central Geological Survey, Geologic map of Taiwan, scale 1:500,000, Central Geological Survey, Ministry of Economic Affairs of Taiwan, 2000.
- Chi, Wu-Cheng, D. Dreger, and A. Kaverina, Finite-source modeling of the 1999 Taiwan (Chi-Chi) Earthquake derived from a dense strong-motion network, *Bull. Seism. Soc. Am.*, 91,



- 1144-1157, 2001.
- Chi, Wu-Cheng and Doug Dreger, Finite fault inversion of the September 25, 1999 (Mw=6.4) Taiwan Earthquake: Implications for GPS displacements of Chi-Chi, Taiwan Earthquake sequence, *Geophys. Res. Lett.*, 29(14), doi:10.1029/2002GL015237, 2002.
- Clark, M. B, D. Fisher, C.-Y. Lu, C.-H. Chen, Kinematic analyses of the Hsuehshan Range, Taiwan; a large-scale pop-up structure Source, *Tectonics*, 12(1), 205-218, 1993.
- Dreger, D., and A. Kaverina, Seismic remote sensing for the earthquake source process and near-source strong shaking: A case Study of the October 16, 1999 Hector Mine Earthquake, *Geophys. Res. Lett.*, 27(13),1941-1944, 2000.
- Hirata, Naoshi, Shin'ichi Sakai, Zen-Sen Liaw, Yi-Ben Tsai, and Shui-Beih Yu, Aftershock observations of the 1999 Chi-Chi, Taiwan earthquake, *Bulletin of the Earthquake Research Institute*, 75(1), 33-46, 2000.
- Hartzell, S.H., and T.H. Heaton, Inversion of strong ground motion and teleseismic waveform data for the fault rupture history of the 1979 Imperial Valley, California, Earthquake, *Bull. Seism. Soc. Am.*, 73, 1553-1583, 1983.
- Hsu, Ya-Ju, Noa Bechor, Paul Segall, Shui-Beih Yu, Long-Chen Kuo, and Kuo-Fong Ma, Rapid afterslip following the 1999 Chi-Chi, Taiwan Earthquake, *Geophys. Res. Lett.*, 29(16), doi:10.1029/2002GL014967, 2002.
- Ji, Chen, Donald V. Helmberger, The-Ru Alex Song, Kuo-Fong Ma, David J. Wald, Slip distribution and tectonic implication of the 1999 Chi-Chi, Taiwan, earthquake, *Geophys. Res. Lett.*, 28(23), 4379-4382, 2001.
- Johnson, K.M, Hsu, Y.J., Segall, P., and Yu, S.B., 2001, Fault geometry and slip distribution of the 1999 Chi-Chi, Taiwan earthquake imaged from inversion of GPS data, *Geophys. Res.*

- Lett.*, 28(11), 2285-2288, 2001.
- Kao, Honn and W.-P. Chen, The Chi-Chi earthquake sequence: active, out-of-sequence thrust faulting in Taiwan, *Science*, 288, 346-2349, 2000.
- Kao, Honn and Jacques Angelier, The Chichi earthquake sequence, Taiwan: results from source parameter and stress tensor inversions, *Sciences de la Terre et des Planetes (Earth and Planetary Sciences)*, 333(1), 65-80, 2001 (in French and English)
- Kikuchi, Masayuki, Yuji Yagi, Yoshiko Yamanaka, Source process of the Chi-Chi, Taiwan earthquake of September 21, 1999 inferred from teleseismic body waves, *Bulletin of the Earthquake Research Institute*, 75(1), 1-13, 2000.
- Lawson, C., and R. Hanson, *Solving Least Squares Problems*, 337 pp., Prentice-Hall, Englewood Cliffs, N.J., 1974.
- Lee, W. H.K., T.C. Shin, K.W. Kuo, K.C. Chen, and C.-F. Wu, CWB free-field strong-motion data from the 21 September Chi-Chi, Taiwan, earthquake, *Bull. Seism. Soc. Am.*, 91(5), 1370-1376, 2001.
- Loevenbruck, Anne, Rodolphe Cattin, Xavier Le Pichon, Marie-Laure Courty, Shui-Beih Yu, Seismic cycle in Taiwan derived from GPS measurements, *Sciences de la Terre et des Planetes (Earth and Planetary Sciences)*, 333(1), 57-64, 2001 (in French and English)
- Lu, Chia-Yu, Hao-Tsu Chu, Jian-Cheng Lee, Yu-Chang Chan, Kuo-Jian Chang, and Frederic Mouthereau, The 1999 Chi-Chi Taiwan earthquake and basement impact thrust kinematics, *Western Pacific Earth Sciences*, 29(2), 181-190, 2002.
- Ma, Kuo-fong, Jim Mori, Shiann-Jong Lee, and Shui-Beih Yu, Spatial and temporal distribution of slip for the 1999 Chi-Chi, Taiwan, earthquake, *Bull. Seism. Soc. Am.*, 91(5), 1069-1087, 2001.

- Ma, Kuo-Fong, The-Ru The, Shiann-Jong Lee, and Hsiang-I Wu, Spatial slip distribution of the September 20, 1999, Chi-Chi, Taiwan, earthquake (Mw 7.6); inverted from teleseismic data, *Geophys. Res. Lett.*, 27(20), 3417-3420, 2000.
- Mori, J. and K.-F. Ma, Slip velocity estimates of the 1999 Chi-Chi, Taiwan Earthquake, New observations of fault dynamics, *Eos Trans. AGU*, U. 81, WP140, 2000.
- Okada, Y., Internal deformation due to shear and tensile faults in a half-space, *Bull. Seism. Soc. Am.*, 82, 1018-1040, 1992.
- Rau, R.-J., and F. Wu, Tomographic imaging of lithospheric structures under Taiwan, *Earth Planet. Sci. Lett.*, 133, 517-532, 1995.
- Saikia, C.K., Modified frequency-wave-number algorithm for regional seismograms using Filon's quadrature-modeling of L(g) waves in eastern North America, *Geophys. J. Int.*, 118, 142-158, 1994.
- Sommerville, P, K. Irikura, R. Graves, S. Sawada, D. Wald, N. Abrahamson, Y. Iwasaki, T. Kagawa, N. Smith, and A. Kowada, Characterizing crustal earthquake slip models for the prediction of strong ground motion, *Seism. Res. Lett.*, 70(1), 59-80, 1999.
- Suppe, John, Mechanics of mountain-building and metamorphism in Taiwan, *Memoir of the Geological Society of China*, 4, 67-89, 1981.
- Suppe, John, Seismic interpretation of the compressively reactivated normal fault near Hsinchu, western Taiwan, *Petroleum Geology of Taiwan*, 20, 85-96, 1984.
- Wald, David J., V. Quitoriane, L.A. Dengler, J.W. Dewey, Utilization of the Internet for rapid community intensity maps, *Seism. Res. Lett.*, 70(6), 680-693, 1999.
- Wang, Wei-Hau and Chau-Huei Chen, Static stress transferred by the 1999 Chi-Chi, Taiwan, earthquake; effects on the stability of the surrounding fault systems and aftershock

- triggering with a 3D fault-slip model, *Bull. Seism. Soc. Am.*, 91(5), 1041-1052, 2001.
- Wang, Chien-Ying, Chien-Li Li, Fu-Chen Su, Ming-Tar Leu, Ming-Shan We, Shao-Huei Lai, and Chir-Cherng Chern, Structural mapping of the 1999 Chi-Chi earthquake fault, Taiwan by seismic reflection methods, *TAO*, 13(3), 211-226, 2002.
- Wu, C, M. Takeo, and S. Ide, Source process of the Chi-Chi earthquake: a joint inversion of strong motion data and Global Positioning System data with a multifault model, *Bull. Seism. Soc. Am.*, 91(5), 1128-1143, 2001.
- Yagi, Y and M. Kikuchi, Source rupture process of the Chi-Chi, Taiwan, Earthquake of 1999, obtained by seismic wave and GPS data, *Eos Trans. AGU*, 81 , WP104, 2000.
- Yu, Shui-Beih, Long-Chen Kuo, Ya-Ju Hsu, Hsuan-Han Su, Chi-Ching Liu, Chin-Shyong Hou, Jiin-Fa Lee, Teng-Chang Lai, Chih-Chung Liu, Cheng-Lun Liu, Teh-Fu Tseng; Chun-Shyong Tsai, and Tzay-Chyn Shin, Preseismic deformation and coseismic displacements associated with the 1999 Chi-Chi, Taiwan, earthquake, *Bull. Seism. Soc. Am.*, 91(5), 995-1012, 2001.
- Zeng, Yeuhua and Chau-Huei Chen, Fault rupture process of the 20 September 1999 Chi-Chi, Taiwan, earthquake, *Bull. Seism. Soc. Am.*, 91(5), 1088-1098, 2001.

## Figure Captions

Figure 1a. Location map. Stars show the locations of the 6 aftershocks. Triangles are the strong motion stations used in the finite source inversions. The numbers below each triangle are the event/events for which this station was used. Surface rupture from the mainshock is plotted for reference. The mainshock asperity is bounded by the towns Sanyi, Puli, and Chusan (Chi et al., 2001). The cross section in the upper left corner shows a schematic with moment tensor solutions for some events of the Chi-Chi earthquake sequence (Kao and Chen, 2000) near these 6 large aftershocks. Two models have been proposed to explain these moment tensor results. Both have an east-dipping decollement represented by the solid line. One model (model 1) proposes another east-dipping fault under the decollement (Kao and Chen, 2000) while another model (model 2) suggests that some of the seismicity below the decollement is on a west-dipping fault (Carena et al., 2002; Chen et al., 2002).

Figure 1b. An enlarge figure from portion of Figure 1a. The stars are the preferred epicenters, which may differ from epicenters reported in other studies. The dot color shows the variance reduction derived from inversions using that particular location as epicenter. It shows how rapidly the waveform fits, measured by variance reduction (VR), deteriorate if the epicentral information is incorrect. Results for Event 5 are shifted to the east for clear presentation. The blue rectangles are the fault dimensions of the preferred slip models. Note that Event 2 and Event 5 are located along the lineation defined by the towns Puli and Chusan. Chi et al. (2001) has proposed that mainshock rupture stopped along this lineation. The cross section in the upper right corner shows a schematic with possible rupture scenarios for the aftershocks we studied. Depending on the causative fault plane and its dip angle, these aftershocks appear to have

ruptured on the decollement, an east-dipping splay fault, a backthrust, or a basement-involved fault.

Figure 2. An example of the particle motion plots we generated to pick stations, to check the consistency of the waveforms with the focal mechanism, and to determine the direction of the horizontal peak ground velocity (HPGV) and the aspect ratio of the particle motion in the populated areas. Filtered observed horizontal waveforms of Event 2 (09201803) were plotted, because this event clearly shows the shear wave radiation pattern for a westward thrusting event. The star shows the hypocenter. The directions of the HPGV, dominated by shear waves and surface waves, are mostly parallel to the backazimuth directions, consistent with a thrust mechanism. A strike-slip mechanism on a vertical fault (e.g. Event 3 of this study) has HPGV directions perpendicular to the backazimuth directions. As a result, the urban region west of the aftershocks experienced mostly E-W strong motion during the thrust-type aftershocks. The aspect ratio is the ratio between the short axis and the long axis of the particle motion ellipse. Note the strong westward directivity of this event.

Figure 3. The slip model for Event 1 (09201757) and its waveform fits. The VR of this slip model is 46% and we assigned low confidence level for this model. The star shows the location of the hypocenter which corresponds to a depth of 8 km and the empty circles are the aftershock seismicity within 5 km of the fault, based on data from the Central Weather Bureau and Kao and Chen (2000). We picked the west-dipping fault as the preferred model because, in addition to the good waveform fits, its slip patch correlates with aftershock seismicity. See Table 2 for parameters and results of this model. The lower panel shows the filtered velocity waveforms as

solid lines and the synthetics as dashed lines. Each time series is 50 sec long and the amplitude of the largest waveform, E component of TCU074, is 0.0269 m/s.

Figure 4. The results of sensitivity tests on the focal mechanism for each event. The P axis of each focal mechanism tested is plotted in lower hemisphere stereonet projection. The left stereonets show the east-dipping fault planes, the right ones the west-dipping planes. The color shows the variance reduction. Note VR deteriorates fastest when the plunge of the P axis changes, implying the waveform fits are most sensitive to the dip, and possibly rake, of the focal mechanism for the thrust events. For the strike-slip aftershock (Event 3), VR is more sensitive to strike. We interpreted this to be the result of the amplitude of the S wave radiation pattern, which controls the inversion results. The star shows the P axis of the preferred focal mechanism.

Figure 5. Variation in the waveform fit derived from sensitivity tests of focal depth, rupture velocity, and dislocation rise time (DRT). The solid lines show the east-dipping faults while the dashed lines are the conjugate west-dipping faults. For event 3 the solid lines are the NW-SE trending faults. Note that VR drops off quickly if the focal depth is more than 5 km from the preferred focal depth. VR is also sensitive to the rupture velocity but less sensitive to dislocation rise time. Event 4 shows evidence of the interrelationship between the causative fault plane, focal depth, and rupture velocity discussed in the text and Figure 10.

Figure 6. The slip model and waveform fits for Event 2 (09201803). The VR of this slip model is 56% and we assigned high level of confidence to this model. The aftershocks are located SW of this east-dipping asperity. The east components of stations TCU078 and TCU079 show

strong directivity effects. The length of the waveforms is 50 sec and the largest amplitude of the waveform is -0.2127 m/s on the E component of TCU078.

Figure 7. Slip model and waveform fits for Event 3 (09202146). The VR of this slip model is 56% and we assigned high confidence level to this model. The focal depth for this event is 18 km but the asperity mainly ruptures at shallow depth in sedimentary layers. This event shows strong evidence of active basement deformation affecting the shallow crust structures. The length of the waveforms is 50 sec and the largest amplitude of the waveform is -0.1046 m/s on the E component of CHY080.

Figure 8. Slip model and waveform fits for Event 4 (09220014). The VR of this slip model is 48% and we assigned a low confidence level to this model. The aftershocks seem to surround the shallow part of the asperity. Many stations east of the epicenter (e.g. all the HWA stations) show surprisingly large amplitudes compared with the western stations, possibly due to a directivity effect from this west-dipping basement fault. The length of the waveforms is 50 sec and the largest amplitude of the waveform is 0.0196 m/s on the E component of TCU129.

Figure 9. Slip model and waveform fits for Event 5 (09252352). The VR of this slip model is 72% and we assigned a high confidence level for this model. The aftershocks are located south of the asperity. The length of the waveforms is 50 sec and the largest amplitude of the waveform is 0.1572 m/s on the E component of TCU078.

Figure 10. Slip model and waveform fits for Event 6 (10220218). The VR of this slip model is



60%. Even though the waveform fits from 14 stations are very good we assigned a low confidence level for this model because we could not determine the causative fault plane conclusively. The aftershock seismicity is also scattered and hard to interpret. The length of the waveforms is 50 sec and the largest amplitude of the waveform is 0.1335 m/s on the E component of CHY009.

Figure 11. Accurate hypocentral depth can help determine the causative fault plane because the conjugate faults may require very different hypocentral depths to fit the waveforms better. Assume we have the correct origin time, epicentral information, focal mechanism, and sufficient information carried in the waveforms to locate the slip in space and time, a reliable hypocentral depth can help determine the causative plane. In this case, a very shallow hypocentral depth (hypocenter 1) will favor a down-dip rupture on the west-dipping fault plane. Also, the optimal rupture velocity on each of the conjugate faults can be used to infer the causative fault plane. That is, the dip of the causative fault plane will control the distance between the hypocenter and slip (rupture distances, marked as L1 and L2 in the figure), thus the preferred rupture velocity. In this case, the shallow east-dipping fault plane will have a shorter rupture distance, and thus a lower rupture velocity. For pure dip-slip rupture, the optimal rupture velocity for the steep-dipping plane divided by the optimal rupture velocity for the shallowly dipping plane is the cotangent of the dip of the shallower dipping fault. For slip not at the updip/down dip location, this becomes an apparent dip problem that involves a bit more algebraic manipulation.

Figure 12. The slip models from this study are plotted on the green topographic contour map. The red dots are the aftershock seismicity from Kao and Chen (2000) and the Central Weather

Bureau. Note Event 5 ruptured just east of Event 2. Event 3 ruptured along NW trend in the aftershock seismicity. The cross section view of the slip model for Event 3 is plotted on the upper left corner.

Figure 13. Post-seismic GPS displacement (Hsu et al., 2002) as large light-colored arrows. Cumulative synthetic GPS displacements derived from the 6 aftershock slip models using Okada's method (1992) as small black arrows. Note the cumulative GPS synthetics can explain at least 80% of the reported post-seismic GPS signals, especially in the southern part of the mainshock rupture where the aftershocks studied are located. One station near  $120.76^{\circ}\text{E}$  and  $23.7^{\circ}\text{N}$  shows opposite directions between the reported and forward-predicted GPS data. This station is near the nodal plane of the strike-slip aftershock (Event 3) so the discrepancy may be due to slight errors in its hypocenter or the strike of the fault.

Table 1: Source parameters and results of the inversions.

Event number	1	2	3	4	5	6
Origin Time	0920/17:57:15.310	0920/18:03:41.160	0920/21:46:37.490	0922/00:14:40.770	0925/23:52:49.509	1022/02:18:56.930
Long	121.01±0.03	120.86±0.03	120.82±0.04	121.08±0.04	121.01±0.03	120.45±0.03
Lat	23.94±0.02	23.81±0.05	23.60±0.04	23.81±0.06	23.87±0.04	23.53±0.04
Depth (km)	8±5	8±4	18±6	10±8	16±7	16±6
M <sub>0</sub> (dyne-cm)	7.15e+024	2.53e+25	2.2e+25	2.5e+25	3.7e+25	1.7e+25
Mw	5.8	6.2	6.2	6.2	6.3	6.1
Strike	200±25	0±20	330±15	165±25	5±15	20±30
Dip	41±25	10±20	89±10	70±25	30±10	75±10
Rake	78±25	80±20	15±15	100±25	100±10	90±15
S/D/R Mw						
Harvard CMT*	N/A	N/A	336/89/1 6.4	183/80/97 6.4	12/20/95 6.5	46/52/125 5.8
NEIC	N/A	N/A	N/A	187/69/108 6.3	N/A	26/55/103 5.9
ERI	N/A	N/A	N/A	175/85/88 6.4	35/25/115 6.4	5/44/74 5.9
BATS	N/A	329/35/59 6.2	242/55/-157 6.3	13/25/124 6.2	50/44/126 6.2	219/29/129 5.9
CHEN (M <sub>f</sub> )	N/A	N/A	N/A	161/69/87 6.8	351/25/60 6.8	N/A
Vrup (km/s)	1.5 (1.3-2.6)	1.6 (1.3-3.5)	2.4 (2.0-2.8)	2.6 (2.0-3.0)	3.2 (1.8-3.6)	2.0 (1.6-2.3)
DRT (sec)	0.2 (0.1-0.6)	0.2 (0.1-0.8)	0.7 (0.2-0.9)	0.7 (0.1-0.9)	0.3 (0.1-0.9)	2.0 (1.6-2.3)
Max Slip (cm)	46	231	85	83	162	205
Str. Drop (MPa)	5.3	6.2	3.8	4.6	5.9	9.9
Asper. Dim	12 x 4	10 x 10	5 x 25	6 x 20	6 x 22	4 x 14
Fault Dim.	24 x 24	14 x 15	24 x 19	24 x 36	30 x 21	18 x 18
# of Stations	13	13	9	9	11	14
VR (%)	46	56	56	48	72	60
Confid. Level	low	high	high	low	high	low
CF S/D/R VR%	35/50/100 48	190/80/92 43	240/75/179 42	318/22/64 23	173/61/84 55	200/15/90 46

(S/D/R: Strike/Dip/Rake; Str. Drop: Stress Drop; Asperity Dimension and Fault Dimension are in km x km; VR: Variance Reduction; CF: conjugate Fault)

Table 2: Parameters Tested in the Inversions

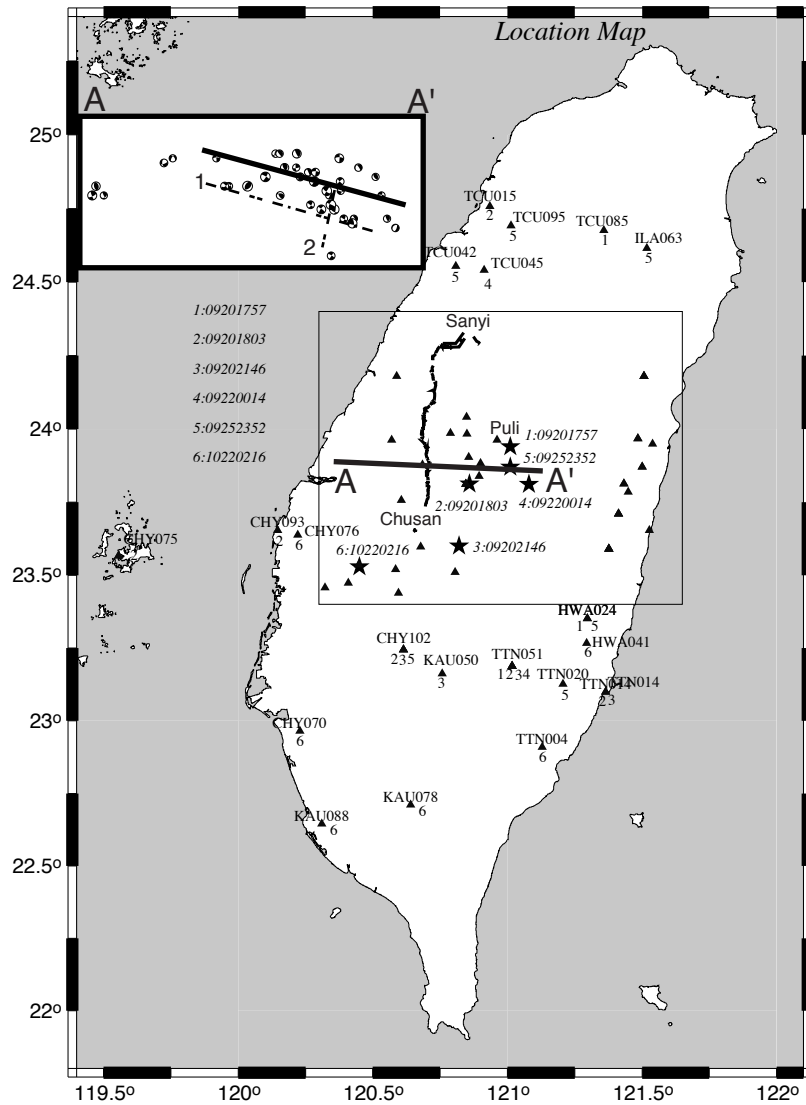
Event number	1	2	3	4	5	6
Origin Time	0920/17:57:15.310	0920/18:03:41.160	0920/21:46:37.490	0922/00:14:40.770	0925/23:52:49.509	1022/02:18:56.930
Long	121.00-121.06 0.01	120.80-120.91 0.01	120.77-120.87 0.01	121.03-121.13 0.01	120.96-121.06 0.01	120.35-120.45 0.01
Lat	23.90-23.96 0.01	23.76-23.86 0.01	23.56-23.65 0.01	23.76-23.86 0.01	23.81-23.91 0.01	23.46-23.56 0.01
Depth (km)	2-30 2	2-30 2	2-24 2	6-34 2	2-30 2	6-26 2
Rup. Vel. (km/s)	0-3.2 0.1	1.0-3.2 0.2	1.0-2.8 0.1	1.0-3.6 0.2	0.2-3.6 0.2	1.0-4.0 0.1
DRT (s)	0.1-1.0 0.1	0.1-1.0 0.1	0.2-1.0 0.1	0.1-1.0 0.1	0.1-0.9 0.1	0.1-0.9 0.1
Strike E-dipping	320 330 340 350 0 10 20 25 30 35 40 50 60	355 0 5 10 15 20 25 30 35 40	310 320 325 330 335 340 350 0	330 340 350 0 10 20	0 5 10 15 20 15 30 35 40	0 10 20 30 40 50 60
Dip E-dipping	10 20 30 40 50 60 70 80	5 10 15 20 25 30 35	80 85 89	10 20 30 40 50 60	10 15 20 25 30 40 45 50 55	50 55 60 65 70 75 80 85
Rake E-dipping	60 70 80 90 100 110 120 130	70 80 85 90 100 110 120	-5 0 5 10 15 20 25 30	70 80 90 100 110 120	085 090 095 100 105 110 115 120 125	60 70 80 90 95 100 110 120 130
Strike W-dipping	150 160 170 180 190 200 210	170 180 190 200 210	185 190 200 210 220 230 240 250	140 145 150 155 160 165 170 190 195 200 205 210 215	160 170 180 190 200 210 220 230	170 180 190 200 210 220
Dip W-dipping	20 30 40 50 60 70 80	45 55 65 75 85	60 70 80 85	40 50 60 65 70 75 80 85	30 40 50 60 70 80	5 10 15 20 25 30 35 40 50
Rake W-dipping	40 50 60 70 80 90 100	70 80 90 100 110 120	140 150 160 170 180	70 80 90 100 110 120	50 60 70 80 90 100	50 60 70 80 90 100 110 120

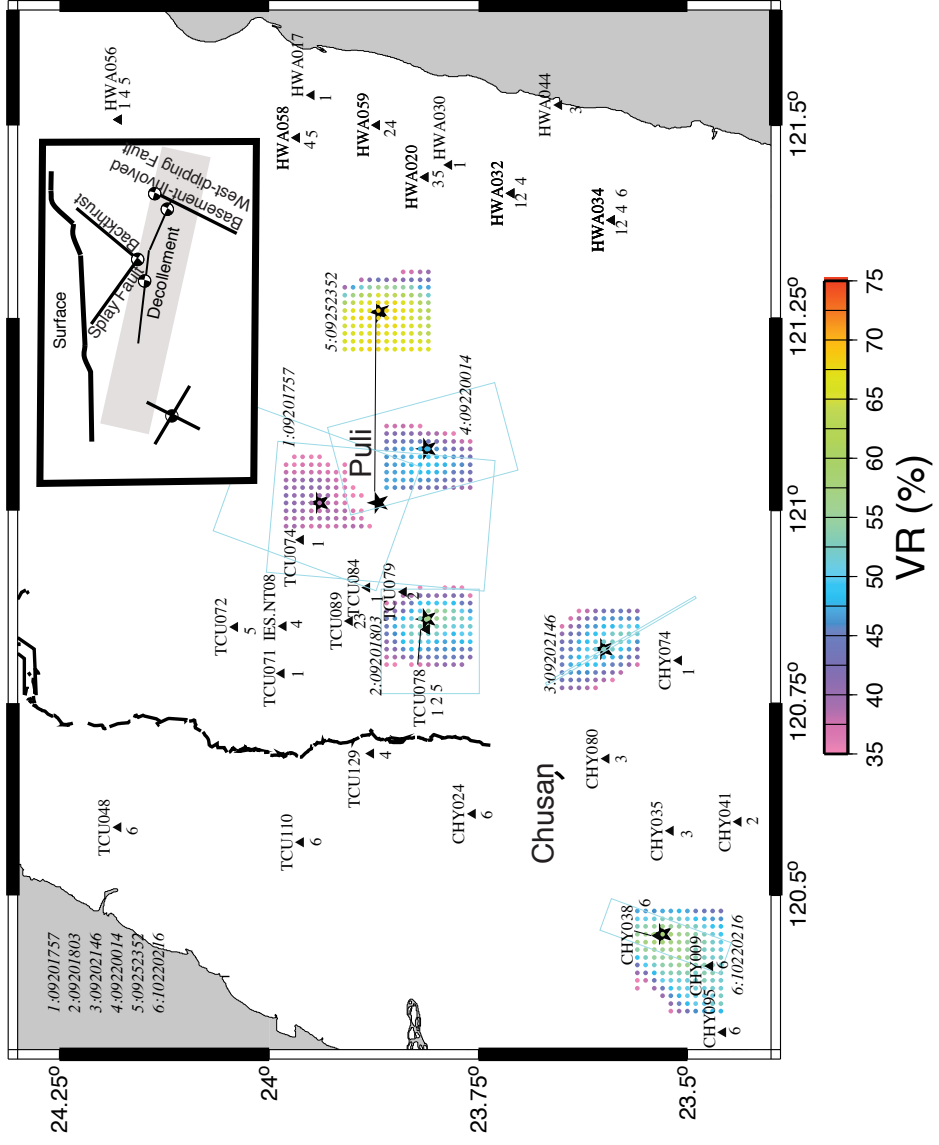
(For latitude, longitude, depth, rupture velocity, dislocation rise time, the formats are: minimum-maximum increment)

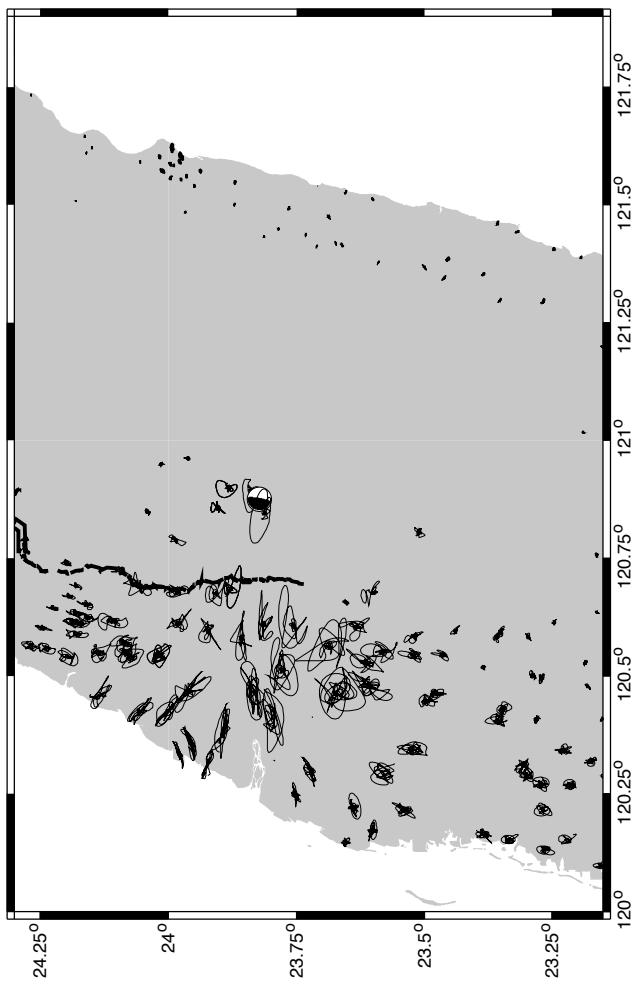
Table 3

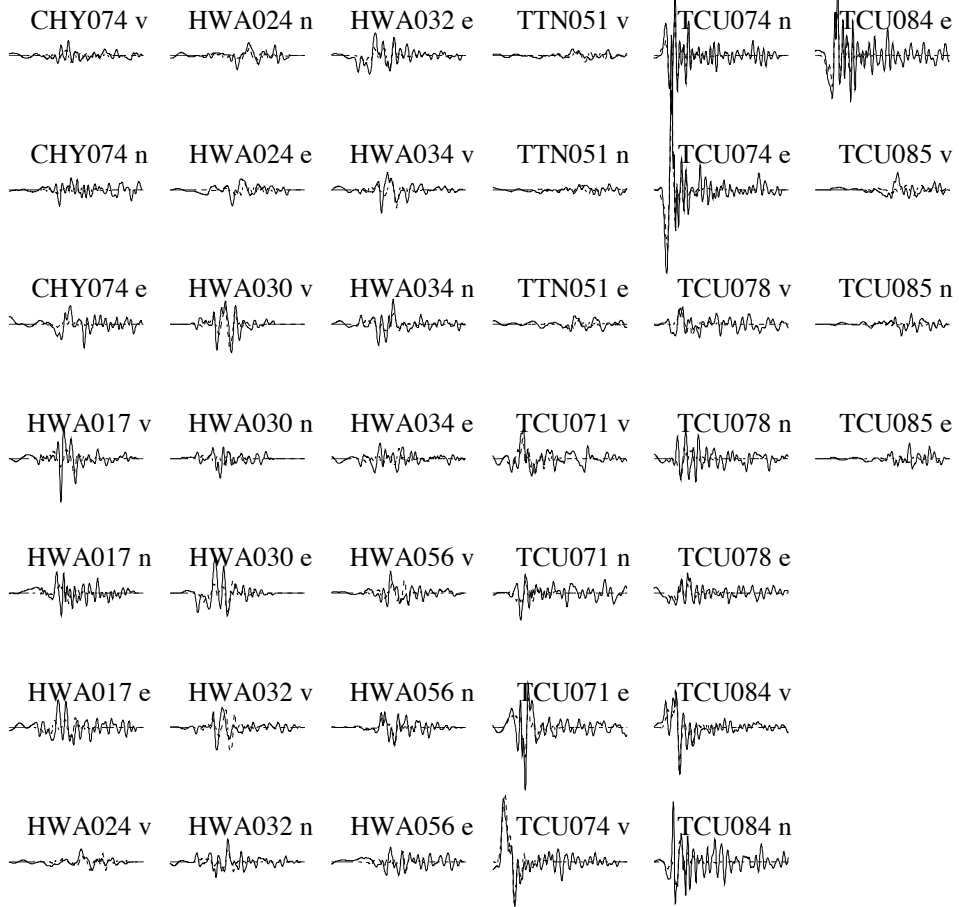
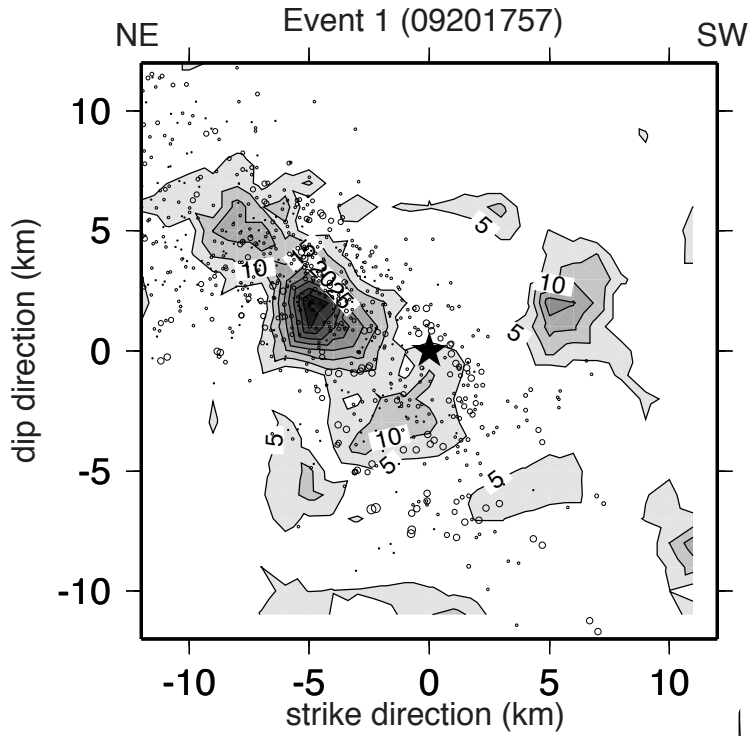
1D velocity model used for Green's function calculation

<i>Thickness</i> (km)	<i>Depth</i> (km)	<i>V<sub>p</sub></i> (km/s)	<i>V<sub>s</sub></i> (km/s)	<i>Density</i> (g/cm <sup>3</sup> )	<i>Q<sub>p</sub></i>	<i>Q<sub>s</sub></i>
2.2	2.2	4.5	2.6	1.8	200	100
2.2	4.4	4.85	2.8	2.05	600	300
2.2	6.6	5.3	3.06	2.25	600	300
2.2	8.8	5.6	3.23	2.39	600	300
4.5	13.3	5.84	3.37	2.5	600	300
4.5	17.8	6.13	3.54	2.64	600	300
7.5	25.3	6.28	3.63	2.7	600	300
8.5	33.8	6.6	3.81	2.85	600	300
5	38.3	6.87	3.97	2.97	600	300
21.5	60.3	7.43	4.29	3.3	600	300
25	85.3	7.8	4.5	3.3	600	300

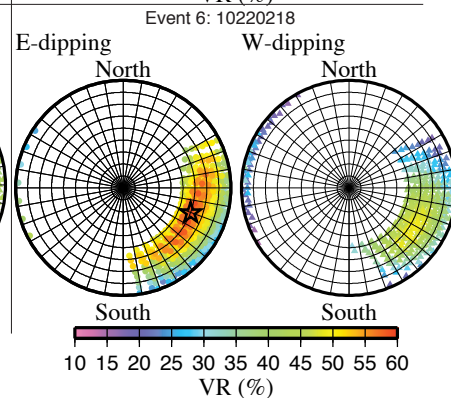
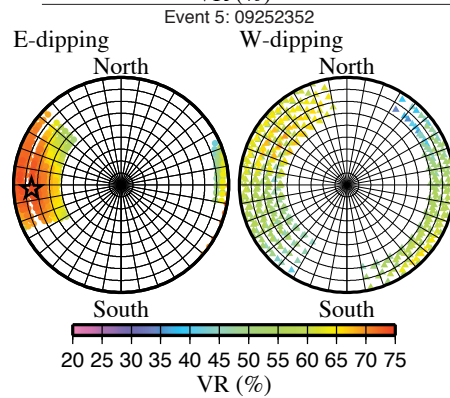
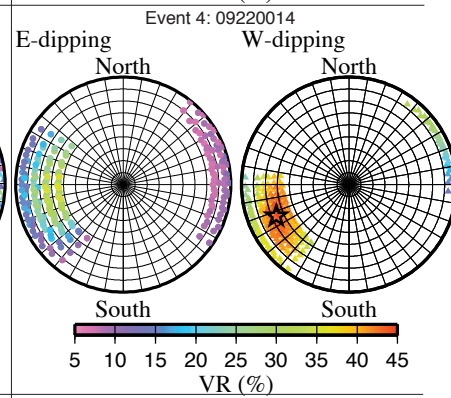
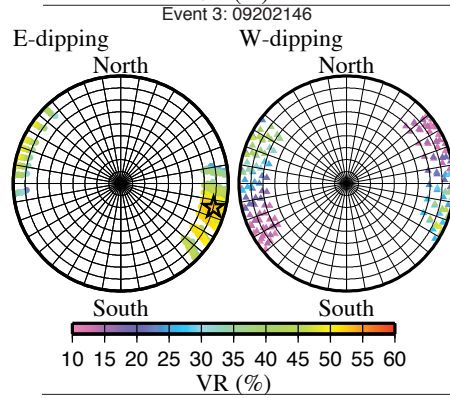
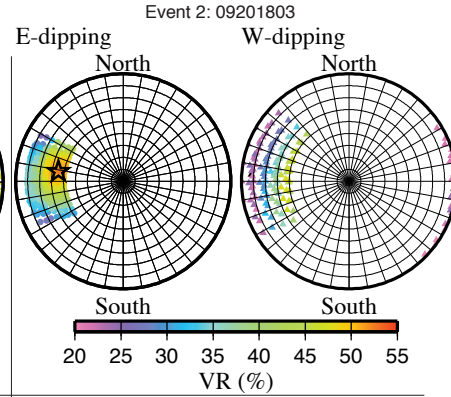
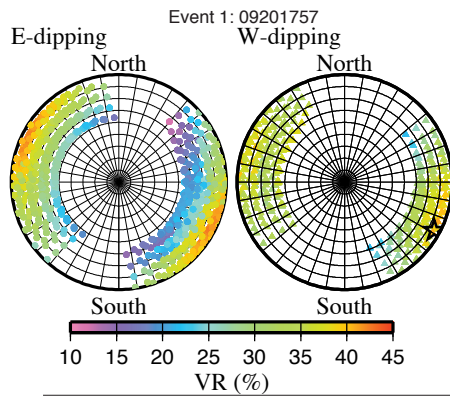


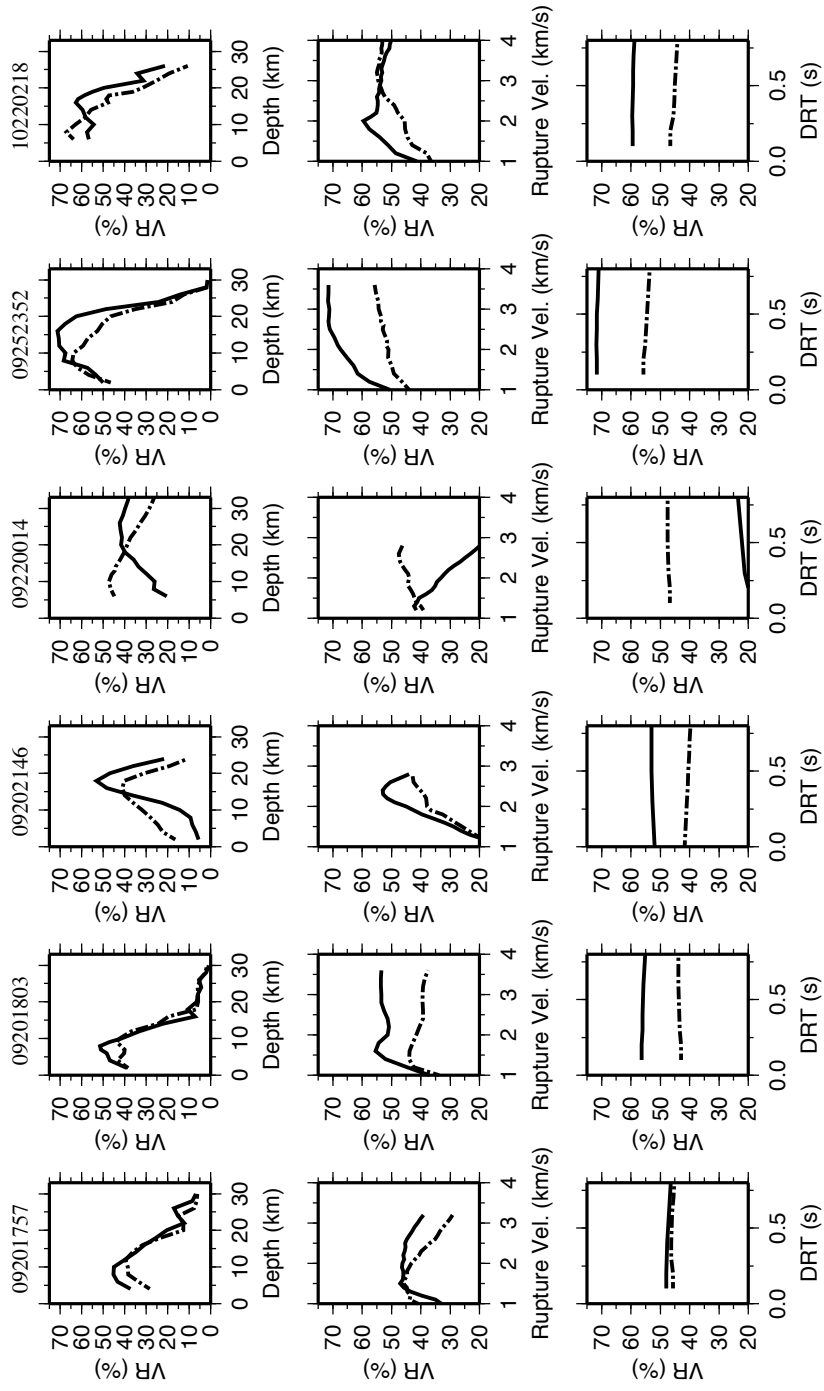




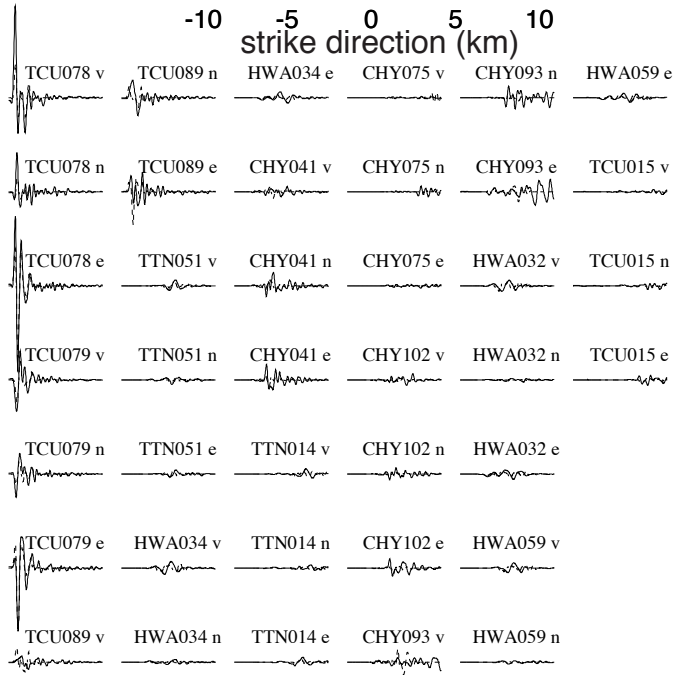
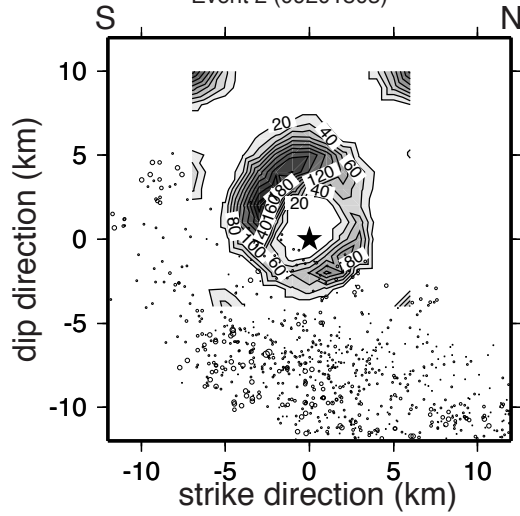


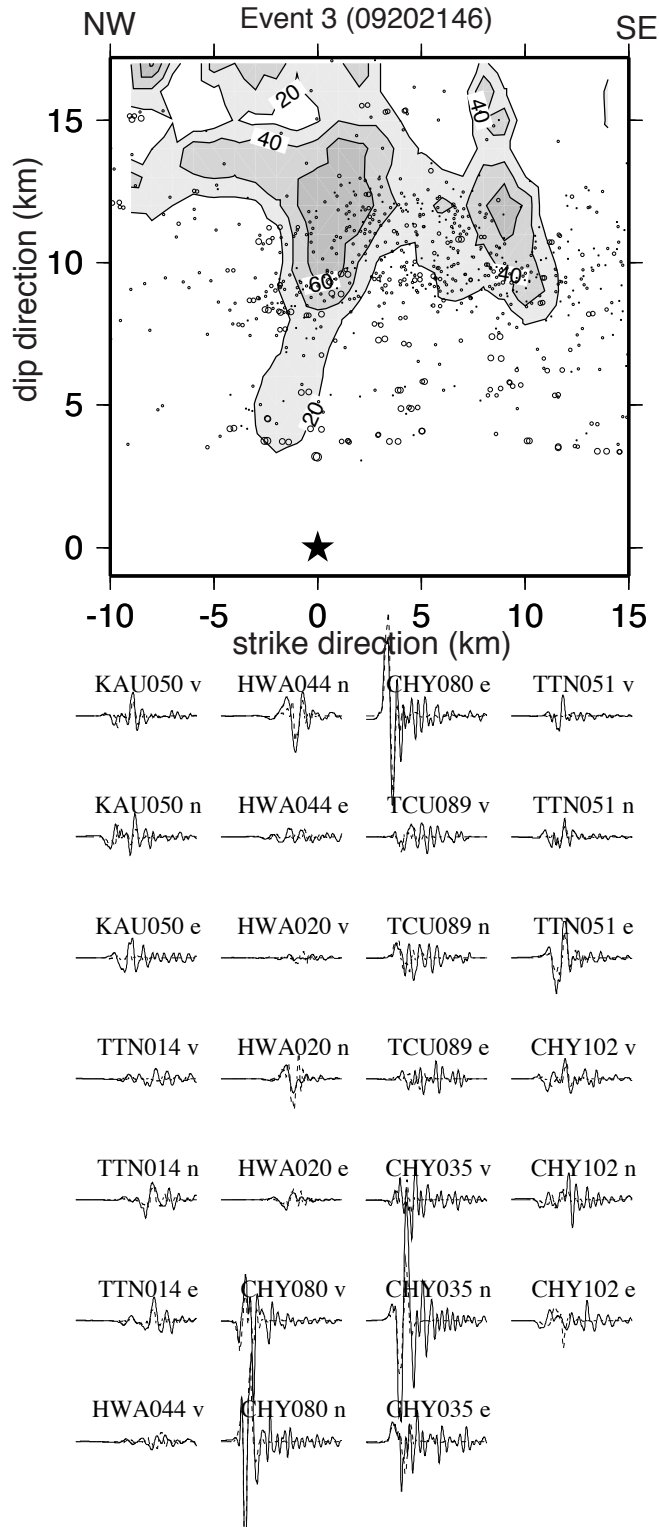


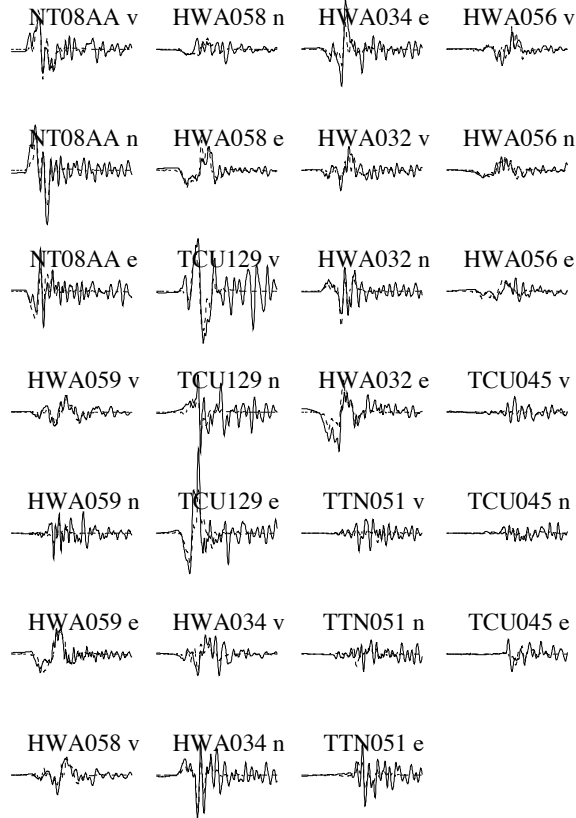
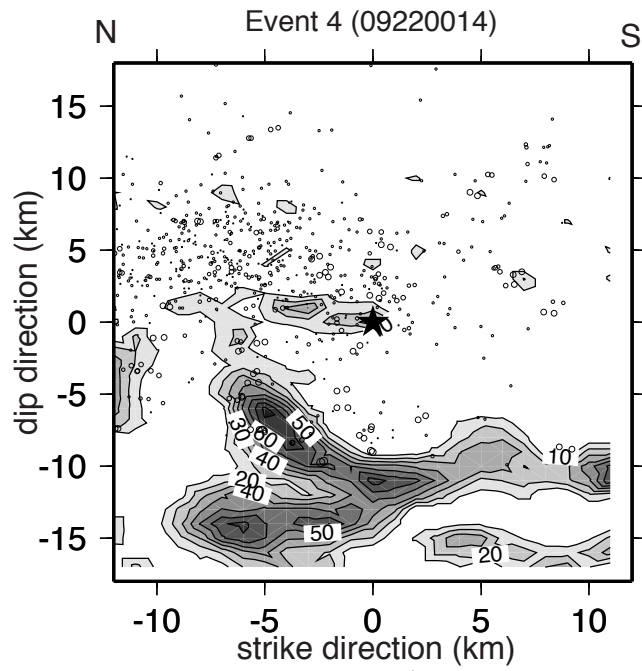


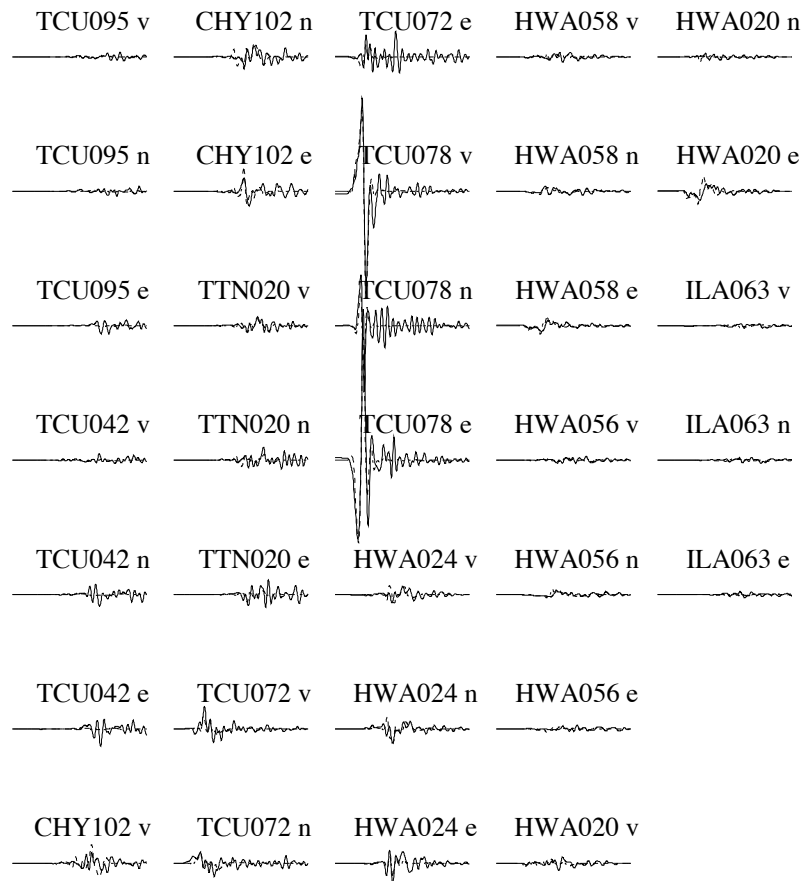
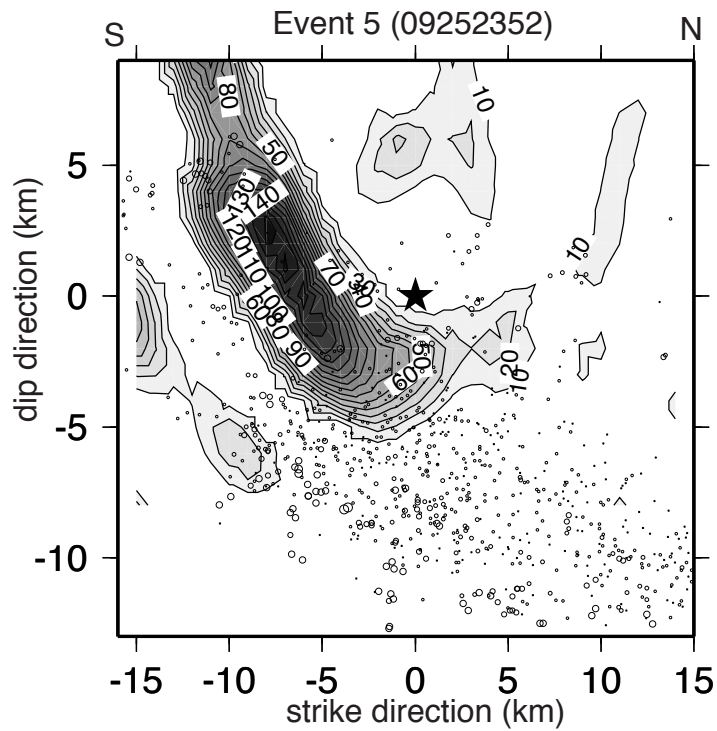


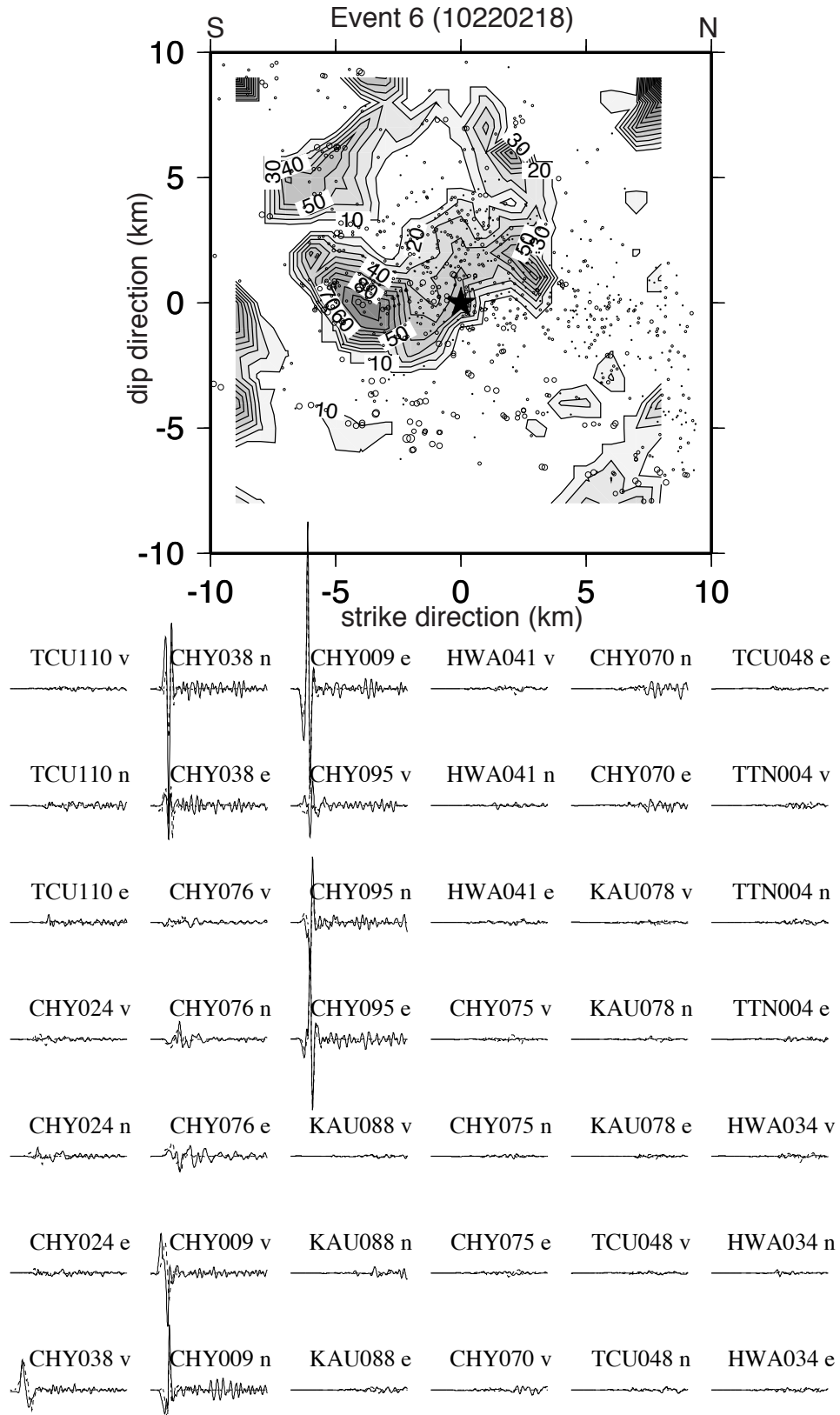
Event 2 (09201803)

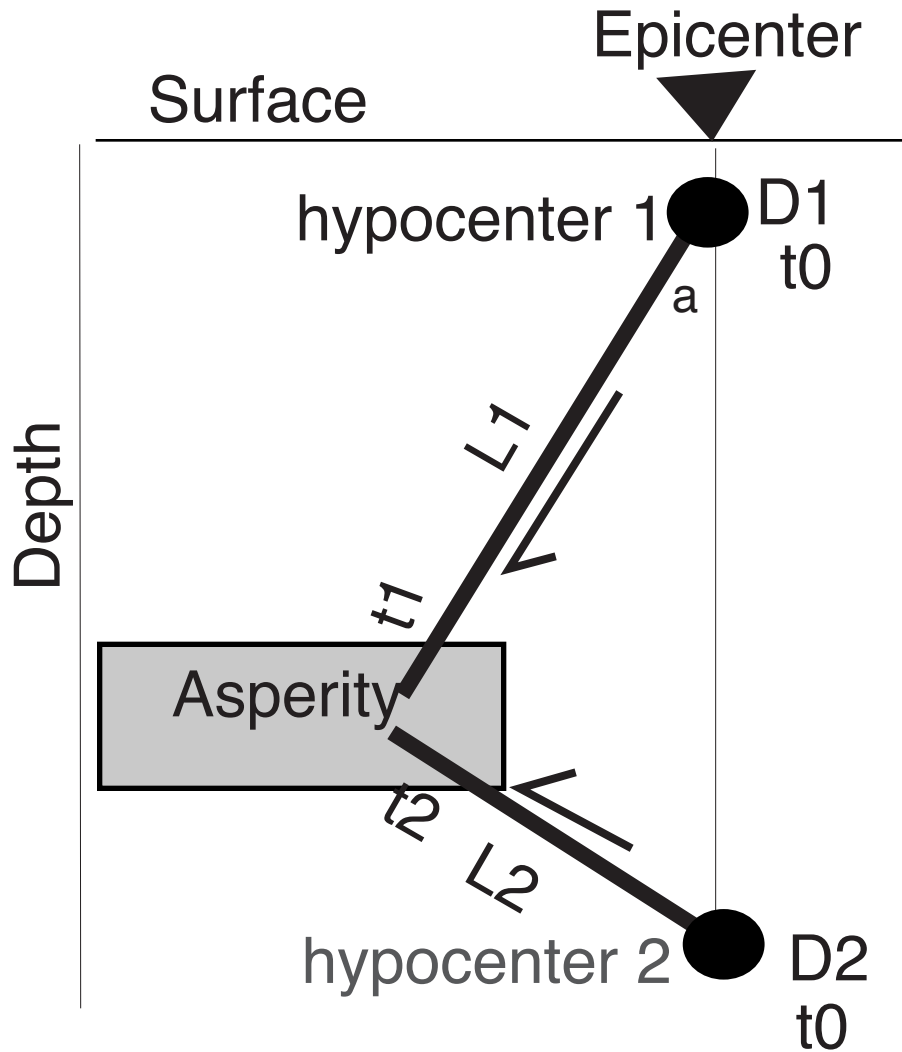












Rupture Vel. ( $V_r$ ) =  $L/(t-t_0)$

$$t_1 = t_2 \quad \frac{L_1}{V_{r1}} = \frac{L_2}{V_{r2}}$$

$$\tan(a) = \frac{L_2}{L_1} = \frac{V_{r2}}{V_{r1}}$$



